

# Rendering 3D Virtual Objects in Mid-Air using Controlled Magnetic Fields

Alaa Adel\*, Mohamed Abou Seif\*, Gerold Hölzl†, Matthias Kranz†, Slim Abdennadher\*, and Islam S. M. Khalil\*

**Abstract**—In this study, we develop an electromagnetic-based haptic interface to provide controlled magnetic forces to the operator through a wearable haptic device (an orthopedic finger splint with single dipole moment) without position feedback. First, we model the electromagnetic forces exerted on a single magnetic dipole attached to the wearable haptic device, and derive magnetic force-current mapping for the dipole moment. Second, this mapping is used as basis for parameter selection of the electromagnetic coils of the haptic interface, dipole moment of the wearable haptic device, and the operating workspace of the system. The electromagnetic-based haptic interface enables three-dimensional (3D) virtual object rendering in mid-air within a workspace of 150 mm × 150 mm × 20 mm, using magnetic forces in excess of 50 mN. Participants experimentally demonstrate a 61% success rate in distinguishing the geometry of 4 representative 3D virtual objects. However, our statistical analysis shows that the ability of the participants to distinguish between geometries is not statistically significant, for 95% confidence level.

## I. INTRODUCTION

One common approach to explore a physical environment is to use relatively transparent bilateral tele-manipulation systems [1]. These systems would allow the operator to interact with an environment at a distance. However, in certain situations, it may not be desirable to achieve direct contact with the environment. For instance, surgical simulation training uses a robotic system to train physicians through video simulations and haptic feedback. This training fosters growth in cognitive and technical capabilities and enhances the standardization of the training requirements for physicians without any contact with the physical environment.

There exist a few challenges that have to be overcome to develop a haptic interface such as the complexity of the mechanical designs, computing power, the real-time response, and the transparency of the position and force feedback during haptic interactions. Electromagnetic systems provide a unique solution to some of the mentioned challenges as the magnetic force and the magnetic torque (exerted on a dipole) are provided at a distance without contact. Therefore, this property decreases the complexity associated with mechanical designs of the existing haptic interfaces [2], [3]. Zhang *et al.* have proposed a magnetic system for rendering volumetric shapes in mid-air for users to perceive

This work was supported by the DAAD-BMBF funding project. The authors also acknowledge the funding from the Science and Technology Development Fund in Egypt (No. 23016).

\*The authors are with the German University in Cairo, New Cairo, Egypt.

†The authors are with the Institute for Embedded Systems, Faculty for Informatics and Mathematics, University of Passau, Passau, Germany.

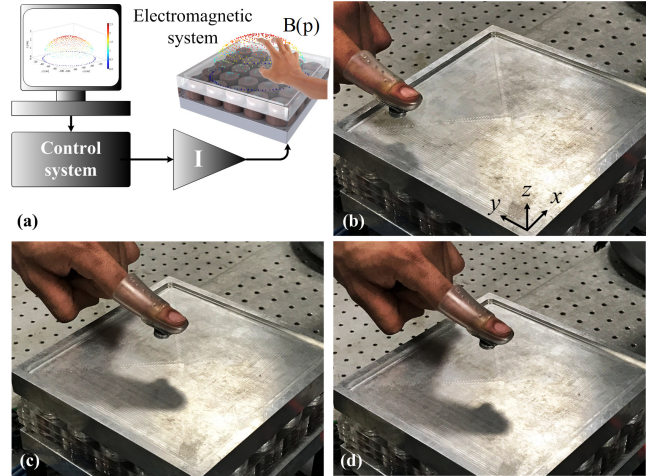


Fig. 1. Electromagnetic-based haptic interface enables the operator to interact with virtual objects in three-dimensional (3D) space. (a) Schematic representation of the electromagnetic-based haptic interface. The system consists of an array of electromagnetic coils. Each coil is powered independently using a current source. A current input ( $\mathbf{I} \in \mathbb{R}^{25 \times 1}$ ) is provided to the coils based on the morphology of a 3D virtual object. The morphology of the object is mapped onto magnetic fields ( $\mathbf{B}(\mathbf{p}) \in \mathbb{R}^{3 \times 1}$ ) and magnetic field gradients to exert magnetic force on a dipole moment (attached to a wearable haptic device) at a position  $\mathbf{p} \in \mathbb{R}^{3 \times 1}$ , respectively. (b), (c), and (d) Magnetic rendering of a hemisphere is achieved and the operator senses the magnetic force via single dipole attached to an orthopedic finger splint.

with attached magnets on the hands [4]. Mid-air tactile sensation generation has also been addressed by wearable haptic devices [5]–[9], air jet (user perceives the air pressure as force) [10], air vortex (effective tactile feedback is provided via air vortex) [11], [12], ultrasound (acoustic radiation pressure is generated using airborne ultrasound transducers) [13], [14], and magnetic force [15], [16]. The ultrasound- and magnetic-based approaches are distinguished by their ability to provide forces at a distance. Brink *et al.* have analyzed the factors affecting the performance, workspace, and stability of untethered magnetic haptic interfaces [17], and have shown the ability of electromagnetic coils without ferromagnetic cores to render relatively stiff virtual surfaces. In this work, we achieve the following:

- Modeling of the magnetic forces exerted on a single dipole and optimization of the current input to decrease the difference between the generated magnetic forces and constraint forces of the virtual object (Fig. 1(a));
- Generation of controlled magnetic forces on a wearable haptic device to provide the operator with force feedback from a virtual object (Figs. 1(b), (c), and (d));

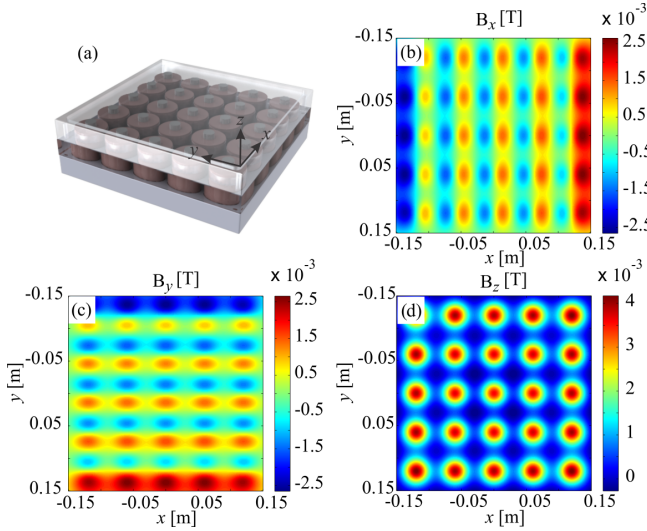


Fig. 2. A representative finite element simulation result of the magnetic fields of the electromagnetic configuration. All electromagnetic coils are supplied with current of 1 A. This configuration generates multiple three-dimensional quadratic functions to render virtual objects. Although the generated magnetic field is in milliTesla range, the corresponding magnetic force at height 20 mm is at order  $\mathcal{O}(10^{-2})$  N. (a) The configuration consists of an array of  $5 \times 5$  electromagnetic coils. (b) Magnetic field along  $x$ -axis. (c) Magnetic field along  $y$ -axis. (d) Magnetic field along  $z$ -axis.

- Measuring the operator's ability to distinguish between various three-dimensional (3D) virtual geometries.

We design, develop, and characterize an electromagnetic-based haptic interface that consists of an array of electromagnetic coils (Fig. 2). These coils generate controlled electromagnetic fields to exert desired magnetic forces [18], [19], [20] on a single magnetic dipole. The magnetic dipole is attached to an orthopedic finger splint to enable the operator to sense the magnetic forces. The remainder of this paper is organized as follows: Section II provides descriptions pertaining to the modeling of the magnetic and constraint forces. Development of the electromagnetic-based haptic device and characterization of its magnetic field, field gradients, and the characteristics of the electromagnetic coils are provided in Section III. Section IV presents our haptic interface experimental results and investigations using one-way ANOVA statistical analysis. Finally, Section VI concludes and provides directions for future work.

## II. SYSTEM DESCRIPTION AND MODELING

Rendering of 3D virtual objects is done using magnetic forces exerted on the dipole of an orthopedic finger splint.

### A. Modeling of the Magnetic Forces

We want to apply controlled magnetic forces on a surface (an orthopedic finger splint) with a single magnetic dipole moment ( $\mathbf{m} \in \mathbb{R}^{3 \times 1}$ ) using a controlled magnetic field  $\mathbf{B}(\mathbf{p}) \in \mathbb{R}^{3 \times 1}$ . Let  $\mathbf{p} \in \mathbb{R}^{3 \times 1}$  be the position of the permanent magnet. If a controlled magnetic field is applied using a configuration of in-plane electromagnetic coils (Fig. 2(a)), then a magnetic force ( $\mathbf{F} \in \mathbb{R}^{3 \times 1}$ ) and torque ( $\mathbf{T} \in \mathbb{R}^{3 \times 1}$ )

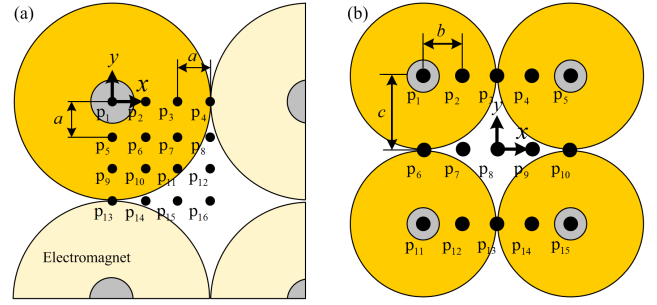


Fig. 3. Measurement of the magnetic field within a grid which spans a limited region of the workspace ( $a=5$  mm,  $b=8$  mm, and  $c=16$  mm) to validate the linearity of the field-current map and theoretical model. The components of the magnetic field are measured at each point of the grid using a calibrated 3-axis digital Teslameter. (a) Single electromagnetic coil is supplied with current input of 1 A. (b) Four electromagnets are supplied independently with current inputs of 1 A. Active and passive coils are indicated using dark and light colors, respectively

are created and are given by [21]

$$\mathbf{F} = V(\mathbf{m} \cdot \nabla) \mathbf{B}(\mathbf{p}) \quad \text{and} \quad \mathbf{T} = V(\mathbf{m} \times \mathbf{B}(\mathbf{p})), \quad (1)$$

where  $V$  is the volume of the permanent magnet. The magnetic force in (1) is given by

$$\mathbf{F} = V \begin{pmatrix} m_x \frac{\partial B_x(\mathbf{p})}{\partial x} + m_y \frac{\partial B_x(\mathbf{p})}{\partial y} + m_z \frac{\partial B_x(\mathbf{p})}{\partial z} \\ m_x \frac{\partial B_y(\mathbf{p})}{\partial x} + m_y \frac{\partial B_y(\mathbf{p})}{\partial y} + m_z \frac{\partial B_y(\mathbf{p})}{\partial z} \\ m_x \frac{\partial B_z(\mathbf{p})}{\partial x} + m_y \frac{\partial B_z(\mathbf{p})}{\partial y} + m_z \frac{\partial B_z(\mathbf{p})}{\partial z} \end{pmatrix}, \quad (2)$$

where  $m_x$ ,  $m_y$ , and  $m_z$  are the components of the net magnetization of the permanent magnet, and  $B_x(\mathbf{p})$ ,  $B_y(\mathbf{p})$ , and  $B_z(\mathbf{p})$  are the components of the external magnetic field along  $x$ -,  $y$ -, and  $z$ -axis, as shown in Figs. 2(b), (c), and (d) and Table I, respectively. These components are mapped onto current ( $\mathbf{I} \in \mathbb{R}^{m \times 1}$ ) input using the following map [22]:

$$\begin{bmatrix} B_x(\mathbf{p}) \\ B_y(\mathbf{p}) \\ B_z(\mathbf{p}) \end{bmatrix} = [\tilde{\mathbf{B}}_x(\mathbf{p}) \quad \tilde{\mathbf{B}}_y(\mathbf{p}) \quad \tilde{\mathbf{B}}_z(\mathbf{p})]^T \mathbf{I}. \quad (3)$$

In (3),  $\tilde{\mathbf{B}}_x(\mathbf{p})$ ,  $\tilde{\mathbf{B}}_y(\mathbf{p})$ , and  $\tilde{\mathbf{B}}_z(\mathbf{p})$  are the magnetic field-current mappings (at point  $\mathbf{p}$ , as shown in Fig. 3) of the field components along  $x$ -,  $y$ -,  $z$ -axis, respectively. Using (3) in (2), we obtain the following force-current map [22]:

$$\begin{aligned} \mathbf{F} &= V \begin{pmatrix} m_x \frac{\partial \tilde{\mathbf{B}}_x(\mathbf{p})}{\partial x} + m_y \frac{\partial \tilde{\mathbf{B}}_x(\mathbf{p})}{\partial y} + m_z \frac{\partial \tilde{\mathbf{B}}_x(\mathbf{p})}{\partial z} \\ m_x \frac{\partial \tilde{\mathbf{B}}_y(\mathbf{p})}{\partial x} + m_y \frac{\partial \tilde{\mathbf{B}}_y(\mathbf{p})}{\partial y} + m_z \frac{\partial \tilde{\mathbf{B}}_y(\mathbf{p})}{\partial z} \\ m_x \frac{\partial \tilde{\mathbf{B}}_z(\mathbf{p})}{\partial x} + m_y \frac{\partial \tilde{\mathbf{B}}_z(\mathbf{p})}{\partial y} + m_z \frac{\partial \tilde{\mathbf{B}}_z(\mathbf{p})}{\partial z} \end{pmatrix} \mathbf{I} \\ &= \mathbf{\Lambda}(\mathbf{m}, \mathbf{p}) \mathbf{I}, \end{aligned} \quad (4)$$

where  $\mathbf{\Lambda}(\mathbf{m}, \mathbf{p}) \in \mathbb{R}^{3 \times m}$  is the magnetic force-current map of the electromagnetic configuration. This mapping provides the magnetic forces exerted on the permanent magnet at position  $\mathbf{p}$ , for a given current input ( $\mathbf{I}$ ). It also enables us to calculate the current input for a desired magnetic force at a point using the following relation:

$$\mathbf{I} = \mathbf{\Lambda}(\mathbf{m}, \mathbf{p})^\dagger \mathbf{F}, \quad (5)$$

TABLE I

EXPERIMENTAL VALIDATION OF THE MAGNETIC FIELD-CURRENT MAP BY CALCULATING THE MAGNITUDES ( $\|\cdot\|$ ) AND ANGLE ( $\angle(\cdot)$ ) DEVIATIONS BETWEEN THE MAGNETIC FIELDS ( $\mathbf{B}$ ) PROVIDED BY (3) AND THE MEASUREMENTS ( $\mathbf{B}_m$ ). SINGLE ELECTROMAGNETIC COIL IS SUPPLIED WITH 1 A. MEASUREMENTS ARE CARRIED OUT AT 16 REPRESENTATIVE POINTS ( $\mathbf{p}_l$  FOR ( $l = 1, \dots, 16$ ) AND ONLY 12 POINTS ARE PROVIDED) WHICH SPAN A SMALL REGION OF THE WORKSPACE (AT HEIGHT OF 14 MM) OF THE SYSTEM USING A CALIBRATED 3-AXIS DIGITAL TESLAMETER.

Point	$\mathbf{p}_1$	$\mathbf{p}_2$	$\mathbf{p}_3$	$\mathbf{p}_5$	$\mathbf{p}_6$	$\mathbf{p}_7$	$\mathbf{p}_9$	$\mathbf{p}_{10}$	$\mathbf{p}_{11}$	$\mathbf{p}_{13}$	$\mathbf{p}_{14}$	$\mathbf{p}_{15}$
$\mathbf{B}_{[mT]}$	$\begin{bmatrix} 0.09 \\ 0.07 \\ 4.6 \end{bmatrix}$	$\begin{bmatrix} 0.08 \\ 1.2 \\ 4.6 \end{bmatrix}$	$\begin{bmatrix} 0.06 \\ 1.8 \\ 3.7 \end{bmatrix}$	$\begin{bmatrix} 1.2 \\ 0.06 \\ 4.1 \end{bmatrix}$	$\begin{bmatrix} 1.1 \\ 1.1 \\ 3.7 \end{bmatrix}$	$\begin{bmatrix} 0.84 \\ 1.6 \\ 3.3 \end{bmatrix}$	$\begin{bmatrix} 1.8 \\ 0.05 \\ 3.1 \end{bmatrix}$	$\begin{bmatrix} 1.6 \\ 0.83 \\ 3.7 \end{bmatrix}$	$\begin{bmatrix} 1.2 \\ 1.3 \\ 2.2 \end{bmatrix}$	$\begin{bmatrix} 1.8 \\ 0.04 \\ 2.1 \end{bmatrix}$	$\begin{bmatrix} 1.7 \\ 0.59 \\ 1.9 \end{bmatrix}$	$\begin{bmatrix} 1.4 \\ 0.97 \\ 1.6 \end{bmatrix}$
$\mathbf{B}_m_{[mT]}$	$\begin{bmatrix} 0.0 \\ 0.0 \\ 4.9 \end{bmatrix}$	$\begin{bmatrix} 0.0 \\ 1.25 \\ 4.6 \end{bmatrix}$	$\begin{bmatrix} 0.0 \\ 2.0 \\ 3.7 \end{bmatrix}$	$\begin{bmatrix} 1.2 \\ 0.0 \\ 4.5 \end{bmatrix}$	$\begin{bmatrix} 1.2 \\ 1.1 \\ 4.3 \end{bmatrix}$	$\begin{bmatrix} 1.05 \\ 1.9 \\ 3.4 \end{bmatrix}$	$\begin{bmatrix} 1.9 \\ 0.0 \\ 3.4 \end{bmatrix}$	$\begin{bmatrix} 1.9 \\ 0.82 \\ 3.3 \end{bmatrix}$	$\begin{bmatrix} 1.63 \\ 1.5 \\ 2.7 \end{bmatrix}$	$\begin{bmatrix} 2.1 \\ 0.0 \\ 2.3 \end{bmatrix}$	$\begin{bmatrix} 2.0 \\ 0.5 \\ 2.3 \end{bmatrix}$	$\begin{bmatrix} 1.8 \\ 1.1 \\ 1.9 \end{bmatrix}$
$\frac{\ \mathbf{B}\ }{\ \mathbf{B}_m\ }$	0.94	0.90	0.85	0.92	0.87	0.83	0.92	0.86	0.82	0.89	0.85	0.82
$\angle(\mathbf{B}, \mathbf{B}_m)$	1.45°	1.56°	2.04°	1.66°	2.26°	0.66°	1.29°	2.32°	1.6°	2.0°	3.93°	2.71°

where  $\mathbf{\Lambda}(\mathbf{m}, \mathbf{p})^\dagger \in \mathbb{R}^{m \times 3}$  is the pseudoinverse of the magnetic-force current map. We use (5) to calculate the current input based on the surface constraint force of the virtual object.

### B. Modeling of the Constraint Force

The virtual object provides equation for the constraint surface,  $g(\mathbf{r}, t) = 0$ . Therefore, the constraint surface results in a constraint force  $\mathbf{f}$  that lay perpendicular to the surface, and is given by

$$\mathbf{f} = \lambda \nabla g(\mathbf{r}, t), \quad (6)$$

where  $\lambda$  is the time-dependent Lagrange multiplier, and  $\mathbf{r} \in \mathbb{R}^{3 \times 1}$  is the position of a point on the constraint surface. Using (4) and (6), the equation of motion of the permanent magnet attached to the wearable haptic device is given by

$$\mathbf{M}\ddot{\mathbf{p}} = \mathbf{F} + \mathbf{f} + \mathbf{f}_h, \quad (7)$$

where  $\mathbf{M}$  is the mass of the permanent magnet and  $\mathbf{f}_h$  is the interaction force between the operator and the permanent magnet (Brink *et al.* have provided a detailed model of this interaction for a single electromagnetic coil [17]). We define an error function ( $\mathbf{e}(\mathbf{I})$ ) between the desired constraint force and the controlled magnetic force using (4) and (6)

$$\mathbf{e}(\mathbf{I}) = \lambda \nabla g(\mathbf{r}, t) - \mathbf{\Lambda}(\mathbf{m}, \mathbf{p})\mathbf{I}. \quad (8)$$

Our objective is to find the optimal current that minimizes the difference between the constraint force and the controlled magnetic force. Therefore, we use (8) to formulate the following optimization objective function:

$$\begin{aligned} & \underset{\mathbf{I}}{\text{minimize}} \quad \varepsilon(\mathbf{I}) = \|\mathbf{e}^T(\mathbf{I})\mathbf{e}(\mathbf{I})\| \\ & \text{subject to} \quad I_i \leq b_i, \quad i = 1, \dots, m. \end{aligned} \quad (9)$$

In (9),  $\varepsilon(\mathbf{I})$  is the scalar objective function to be minimized using  $\mathbf{I}$ . Further,  $I_i$  is the input current to the  $i$ th electromagnetic coil, and  $b_i$  is an upper-limit on the input current. The configuration of the electromagnetic coils enables generation of multiple 3D quadratic functions, as shown in Fig. 2(d). Increasing the number of these functions

improves the magnetic rendering quality of the 3D virtual objects. Therefore, we approximate the generated field using the following Gaussian function:

$$f(x, y) = \sum_{i=1}^m A_i \exp \left( -\frac{(x - x_{oi})^2}{2\sigma_{xi}^2} - \frac{(y - y_{oi})^2}{2\sigma_{yi}^2} \right), \quad (10)$$

where  $A_i$  is the amplitude of the Gaussian function (centered at  $x_{oi}$  and  $y_{oi}$ ) generated by  $i$ th electromagnetic coils, for  $i = 1, \dots, m$ , and  $m$  is the number of coils within the electromagnetic configuration. Further,  $\sigma_{xi}$  and  $\sigma_{yi}$  are the  $x$  and  $y$  spreads of the  $i$ th quadratic function, respectively. The amplitude  $A_i$  of the  $i$ th Gaussian function is controlled using the  $I_i$  current input, whereas the spreads ( $\sigma_{xi}$  and  $\sigma_{yi}$ ) depend on the geometry of the coil. Therefore, the ability of the electromagnetic configuration to render a 3D surface is measured using a rendering index ( $RI$ ) calculated using the following steps: (1) Discretization of the 3D geometry and calculation of the corresponding constraint force using (6). (2) Values of the constraint force are mapped onto the range (0,1) using,  $\hat{\mathbf{f}} = \frac{\mathbf{f}}{\max(\mathbf{f})}$ , where  $\hat{\mathbf{f}}$  is the normalized constraint force. (3) The generated magnetic forces are also mapped onto the range (0,1) using,  $\hat{\mathbf{F}} = \frac{\mathbf{F}}{\max(\mathbf{F})}$ , where  $\hat{\mathbf{F}}$  is the normalized magnetic force of the 3D object. (4) The rendering index is calculated as the mean absolute error of the normalized constraint and magnetic forces as follows:

$$RI = \frac{1}{n} \sum |\hat{\mathbf{f}} - \hat{\mathbf{F}}|, \quad (11)$$

where  $n$  is the length of the force vectors. The rendering index reflects the ability of the electromagnetic configuration to render a 3D virtual objects using a limited number ( $m$ ) of coils, and is calculated during our experimental validation for each geometry.

## III. ELECTROMAGNETIC-BASED HAPTIC INTERFACE

Our system consists of an array of electromagnetic coils. We develop the system and characterize its properties.

TABLE II

EXPERIMENTAL VALIDATION OF THE MAGNETIC FIELD-CURRENT MAP BY CALCULATING THE MAGNITUDES ( $\|\cdot\|$ ) AND ANGLE ( $\angle(\cdot)$ ) DEVIATIONS BETWEEN THE MAGNETIC FIELDS ( $\mathbf{B}$ ) PROVIDED BY (3) AND THE MEASUREMENTS ( $\mathbf{B}_m$ ). FOUR ELECTROMAGNETIC COILS ARE SUPPLIED WITH CURRENT INPUTS OF 1 A. MEASUREMENTS ARE CARRIED OUT AT 15 REPRESENTATIVE POINTS ( $\mathbf{p}_l$  FOR  $l = 1, \dots, 15$ ) AND ONLY 11 POINTS ARE PROVIDED) WHICH SPAN A SMALL REGION OF WORKSPACE (AT HEIGHT OF 18 MM) OF THE MAGNETIC SYSTEM.

Point	$\mathbf{p}_1$	$\mathbf{p}_2$	$\mathbf{p}_3$	$\mathbf{p}_4$	$\mathbf{p}_5$	$\mathbf{p}_6$	$\mathbf{p}_7$	$\mathbf{p}_8$	$\mathbf{p}_9$	$\mathbf{p}_{10}$	$\mathbf{p}_{11}$
$\mathbf{B}_{[mT]}$	$\begin{bmatrix} -1.2 \\ -1.3 \\ 4.2 \end{bmatrix}$	$\begin{bmatrix} -0.3 \\ -1.4 \\ 4.1 \end{bmatrix}$	$\begin{bmatrix} 0.0 \\ -1.4 \\ 3.9 \end{bmatrix}$	$\begin{bmatrix} 0.4 \\ -1.4 \\ 4.1 \end{bmatrix}$	$\begin{bmatrix} 1.3 \\ -1.3 \\ 4.1 \end{bmatrix}$	$\begin{bmatrix} -1.3 \\ 0.0 \\ 4.0 \end{bmatrix}$	$\begin{bmatrix} -0.4 \\ 0.0 \\ 4.1 \end{bmatrix}$	$\begin{bmatrix} 0.0 \\ 0.0 \\ 4.0 \end{bmatrix}$	$\begin{bmatrix} 0.5 \\ 0.0 \\ 4.1 \end{bmatrix}$	$\begin{bmatrix} 1.4 \\ 0.0 \\ 3.9 \end{bmatrix}$	$\begin{bmatrix} -1.2 \\ 1.2 \\ 4.2 \end{bmatrix}$
$\mathbf{B}_m_{[mT]}$	$\begin{bmatrix} -1.0 \\ -1.4 \\ 3.6 \end{bmatrix}$	$\begin{bmatrix} -0.3 \\ -1.4 \\ 3.7 \end{bmatrix}$	$\begin{bmatrix} 0.0 \\ -1.4 \\ 3.7 \end{bmatrix}$	$\begin{bmatrix} 0.3 \\ -1.4 \\ 4.3 \end{bmatrix}$	$\begin{bmatrix} 1.2 \\ -1.3 \\ 4.3 \end{bmatrix}$	$\begin{bmatrix} -1.2 \\ -0.3 \\ 3.7 \end{bmatrix}$	$\begin{bmatrix} -0.5 \\ -0.2 \\ 3.8 \end{bmatrix}$	$\begin{bmatrix} 0.0 \\ 0.0 \\ 3.8 \end{bmatrix}$	$\begin{bmatrix} 0.4 \\ 0.0 \\ 4.0 \end{bmatrix}$	$\begin{bmatrix} 1.2 \\ 0.2 \\ 3.9 \end{bmatrix}$	$\begin{bmatrix} -1.3 \\ 0.8 \\ 4.4 \end{bmatrix}$
$\frac{\ \mathbf{B}\ }{\ \mathbf{B}_m\ }$	1.14	1.09	1.05	1.02	0.96	1.07	1.07	1.05	1.03	0.99	0.97
$\angle(\mathbf{B}, \mathbf{B}_m)$	3.92°	1.93°	0.97°	0.76°	2.19°	5.16°	3.23°	0.0°	1.88°	4.44°	5.73°

### A. System Development

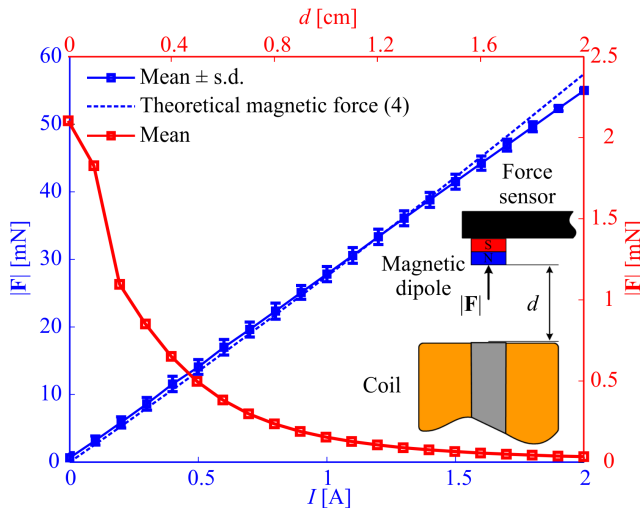
Each electromagnetic coil has inner- and outer-diameters of 10 mm and 29.2 mm, respectively. The height of the coil and the length of its low carbon steel core (with relatively low residual magnetism) are 37.6 mm and 51.3 mm, respectively. The wire thickness and the number of turns are 0.7 mm and 737, respectively. Each of the electromagnets is independently supplied with current using electric drivers (MD10C, Cytron Technologies Sdn. Bhd, Kuala Lumpur, Malaysia) and controlled via an Arduino control board (Arduino UNO - R3, Arduino, Memphis, Tennessee, U.S.A). The electromagnetic coils are fixed to an upper and lower aluminum frames to keep all magnetization axes parallel to each other. The electromagnetic configuration provides a planar footprint of 15 cm  $\times$  15 cm, whereas the height of this footprint is limited to 20 mm due to the limited projection distance of the magnetic field and magnetic field gradient. We use the magnetic field-current map (3) to simulate the magnetic fields along  $x$ -,  $y$ -, and  $z$ -axis, as shown in Figs. 2(b), (c), and (d), respectively. These fields induce magnetic torque on the magnetic dipole moment of the orthopedic finger splint. The permanent magnet (NdFeB) has diameter and length of 12 mm and 2 mm, respectively, with axial magnetization of  $7.95 \times 10^5$  A.m $^{-1}$ . The magnetic field generated within the workspace of the electromagnetic configuration is at order  $\mathcal{O}(10^{-3})$  T. Therefore, the magnetic torque exerted on the permanent magnet has an upper-limit at order  $\mathcal{O}(10^{-4})$  N.m. We also calculate the magnetic field gradient using (1). The electromagnetic system provides magnetic field gradient at order  $\mathcal{O}(10^{-2})$  T.m $^{-1}$ , and hence the magnetic force has an upper-limit at order  $\mathcal{O}(10^{-2})$  N (at approximately 20 mm along  $z$ -axis). This force is greater than the minimum force of our sensory range (approximately 0.8 mN [23]), and therefore we limit the height of the workspace to 20 mm.

### B. System Characterization

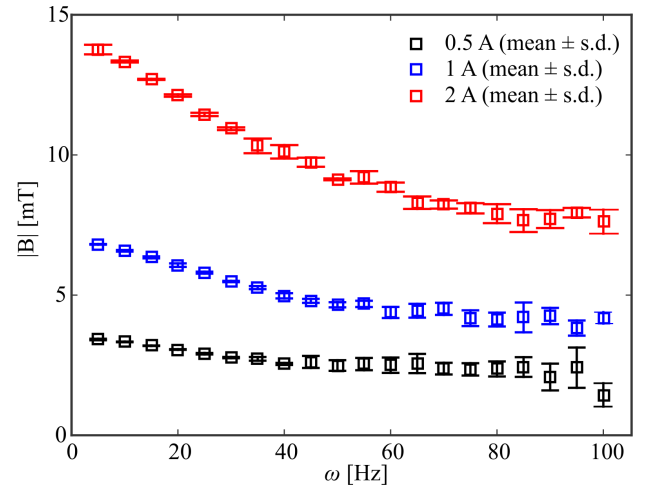
We use a calibrated 3-axis digital Teslometer (Senis AG, 3MH3A-0.1%-200mT, Neuhofstrasse, Switzerland) to verify the accuracy of the mathematical models (1), (3) and (4).

A grid of 15 representative points is defined at height  $h=2$  cm, from the electromagnetic coil and the magnetic field is measured at the points shown in Fig. 3(a). The measured ( $\mathbf{B}_m$ ) and simulated magnetic fields are included in Table I, for current input of 1 A to a single electromagnetic coil. The deviations in magnitude ( $\frac{\|\mathbf{B}\|}{\|\mathbf{B}_m\|}$ ) and in orientation ( $\angle(\mathbf{B}, \mathbf{B}_m)$ ) allow us to verify that maximum error in magnitude and orientation are 20% and 3.93°, respectively. The linearity of the magnetic field-current map allows us to superimpose the magnetic field generated using each coil, and therefore the measurements of the magnetic field is done by activating 4 electromagnetic coils, as shown in Fig. 3(b). Each of the electromagnetic coils is provided with current input of 1 A, and the corresponding measured and calculated magnetic fields are provided in Table II. The maximum deviations in magnitude and in orientation of the calculated fields are calculated to be 4% and 5.16°, respectively.

The controlled magnetic forces are exerted on an NdFeB permanent magnet. We measure the magnetic force at different current inputs between 0 A to 2 A, as shown in Fig. 4(a), using a force sensor (ABS-N/ABJ-NM, Mechanikus Gottlieb KERN, Balingen, Germany). The measurements are also compared to the theoretical magnetic force calculated using (4), using single electromagnetic coil. Despite the deviation (in magnitude and direction) between the measured and calculated magnetic fields, we find reasonable agreement (within the measurement error) between the calculated and measured magnetic forces for current inputs below 1.6 A. We also limit the workspace of the electromagnetic configuration within a height of 22.5 mm. This limitation is based on the projection distance of the magnetic force, as shown in Fig. 4(a). It is likely that the virtual object will have time-dependent geometry ( $g(\mathbf{r}, t)$ ), and hence the response of the coils to time-varying current input is characterized. Fig. 4(b) shows the frequency response of an electromagnetic coil to a sinusoidal current input. We calculate the magnetic field at a point (with height  $h = 14$  mm) for current inputs of 0.5 A, 1.0 A, and 2.0 A throughout a frequency range of 0 Hz to 100 Hz. At frequencies of approximately 85 Hz,



(a) Magnetic force versus input current and distance.



(b) Frequency response of the coil.

Fig. 4. The magnetic force ( $|F|$ ) exerted on a magnetic dipole is measured and compared to the theoretical force using (4). The force is measured at height of 20 mm on a permanent magnet (NdFeB) with diameter and length of 12 mm and 2 mm, respectively, and axial magnetization of  $7.95 \times 10^5 \text{ A.m}^{-1}$ . The average and standard deviation (s.d.) are calculated using 5 trials at every current input. The projected magnetic force is 33 mN at distance of 22.5 mm. The magnetic force is measured using a force sensor (ABS-N/ABJ-NM, Mechanikus Gottlieb KERN, Balingen, Germany) (b) Frequency response of an electromagnetic coil is calculated for 3 representative current inputs (0.5 A, 1 A, and 2 A). At frequencies ( $\omega$ ) of approximately 85 Hz, 95 Hz, and 100 Hz, the magnetic field drops by 50%, for current inputs ( $I$ ) of 0.5 A, 1.0 A, and 2.0 A, respectively.

95 Hz, and 100 Hz, the magnetic field drops by 50%, for current inputs of 0.5 A, 1.0 A, and 2.0 A, respectively. The frequency response of the electromagnetic coils suggests that we would obtain almost uniform magnetic fields using relatively low current input. This uniformity is not preserved at current input of 2.0 A. In this experiment the means and standard deviations (s.d.) are calculated using 5 trials at each frequency and each current input.

#### IV. SENSING 3D VIRTUAL OBJECTS

We experimentally evaluate the ability to of the system to render 3D objects. First, we render various geometries. Second, data is collected from 10 participants.

##### A. Rendering 3D Virtual Objects

The magnetic rendering of a virtual 3D object is done by generating its surface constraint ( $g(\mathbf{r}, t)$ ) using a computer-aided design software (SOLIDWORKS, Dassault Systèmes SOLIDWORKS Corp., Massachusetts, U.S.A). The surface constraint is discretized into 3D points. Fig. 5(a) shows 2601 points that span a flat surface. A constraint force at each of these points is calculated using (6), as shown in Fig. 5(b). The constraint forces are calculated at the small black circles and a surface fit is added, and represents the desired constraint force that enables the operator to interact with the virtual flat surface. The generated magnetic fields and magnetic field gradients are shown in Figs. 5(c), (d), (e), and (f), respectively. The presence of a permanent magnet within the orthopedic finger splint produces a magnetic force, as shown in Fig. 5(g). Finally, Fig. 5(h) shows the input current to the 25 electromagnetic coils of the electromagnetic-based haptic interface. Figs. 5(b) and (g) show the desired constraint force and the exerted magnetic force. There exist

a difference between these two forces owing to the limited number of electromagnetic coils. These coils generate several local maxima (represented using (10)) that render the desired shape of a virtual object.

We repeat the mentioned procedure on a virtual hemisphere (the sphere has diameter of 300 mm and its center is located at  $-130 \text{ mm}$  along  $z$ -axis), as shown in Fig. 6. The discretized constraint surface and the desired constraint forces are indicated using the small blue and black circles, respectively (Figs. 6(a) and (b)). The corresponding magnetic fields along  $x$ -,  $y$ -, and  $z$ -axis are calculated, as shown in Figs. 6(c), (d), and (e), and the magnetic field gradient is determined (Fig. 6(f)). Finally, the generated magnetic force is provided in Fig. 6(g). The current inputs supplied to the electromagnetic coils are calculated using (9). The optimization is performed using the Levenberg-Marquardt algorithm from MATLAB 8.4 (R2014b, The MathWorks, Inc., Massachusetts, USA). Fig. 7 shows the number of iterations used to render the flat surface and the hemisphere. After 4 iterations the rendering index (11) converges to an asymptote and current inputs are calculated.

##### B. Preliminary Validation and Statistical Analysis

In order to validate the electromagnetic-based haptic interface experimentally, we devise a set of experiments for ten participants. The experiments include 200 randomly rendered force trials, for the ten participants (males and females, average age of 24). The ten participants slide their fingers over the virtual objects and are asked to distinguish between four 3D geometries, i.e., flat surface, hemisphere, wedge, and hemicylinder. At the end of each trial, the participants are asked to provide their confidence of the type of geometry (Table III). In each trial, participants are instructed to



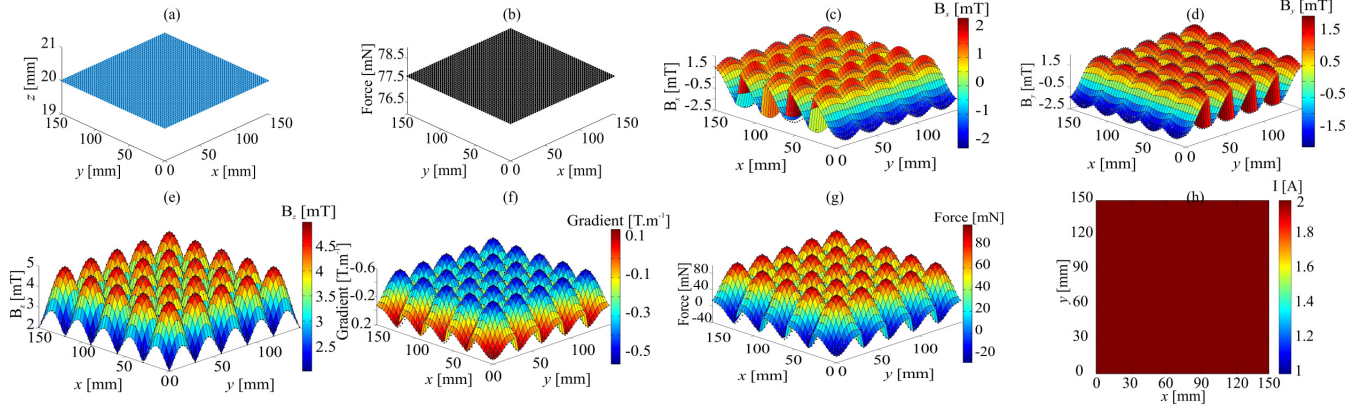


Fig. 5. Magnetic rendering of a flat surface (at height of 20 mm) is achieved. (a) The surface constraint ( $g(\mathbf{r}, t)$ ) of the half sphere is decomposed into 2601 points. (b) The constraint force (6) is calculated based on the surface constraint and the scalar  $\lambda$ . (c, d, and e) Magnetic fields along  $x$ -,  $y$ -, and  $z$ -axis are calculated using (2) based on the constraint force. (f) The magnetic field gradient is also generated using (2). (g) Magnetic forces are calculated and generated using (4) and (5). (h) The current inputs to the coils are calculated using (9). The rendering index of the flat surface is 0.45 mN.

select between the four 3D geometries that are generated randomly using our control system. All participants use the electromagnetic-based haptic interface for the first time and they are not involved again in any of the trials. We observe that the skills of the participants grow with time and their ability to distinguish between the geometries increase with every trial. Therefore, we limit the number of trials of each participant to 20 trials. Table III provides the accuracy of each geometry for each participant. We devise the following null ( $H_0$ ) and alternative ( $H_a$ ) hypothesis:

- $H_0$ : The difference between the means of the geometries is not statistically significant;
- $H_a$ : The difference between the means of the geometries is statistically significant.

The data in Table III is examined using one-way ANOVA analysis to determine the successful trials with confidence level of 95% ( $\alpha = 5\%$ ). Our experimental data are normally distributed based on Anderson-Darling and Ryan-Joiner tests, and are collected randomly (data of all geometries except the flat surface have normal distribution). Finally, the variances of each geometry are equal, and we can assume homogeneity of variance. The ANOVA analysis suggests  $p\text{-value}=0.15 > \alpha$ , and therefore we accept the null-hypothesis and reject the alternative hypothesis. There is no evidence to conclude that the difference among the mean of accuracy for the four geometries is significant, at  $\alpha=0.05$  and 95% confidence level. We attribute this result to a few factors. First, the participants use single magnetic dipole moment and slide their finger to decide on the rendered geometry. Increasing the number of dipole moments within the wearable haptic device or using multiple orthopedic finger splints would improve the ability of the user to differentiate between the rendered magnetic forces. Second, the limited number of electromagnetic coils also influences the rendering resolution and the decisions of the participants. Third, the number of trials of each participants also affects our statistical analysis. This number is limited to provide correct validation of the electromagnetic-based haptic interface (as the participants

achieve more successful trials with time).

## V. DISCUSSIONS

Rendering of 3D virtual objects in mid-air using magnetic force exerted on single dipole moment is demonstrated. Our experiments show that participants can distinguish between four geometries based on single dipole moment attached to an orthopedic finger splint. The experimental data provided in Table III indicates that participants achieve 61% success rate in distinguishing between the four different geometries. However, our statistical analysis reveals that there is no significance between the different geometries. Although it is suggested that more experimental trials have to be included to enhance the statistical analysis, the number of trials of each participant is limited to 20 (approximately 5 trials for each geometry) as we observe that participants achieve greater success rates in the last trials, as opposed to the first few trials. Participants have a prior knowledge pertaining to the shapes only and are not informed about the results during their consecutive trials. In addition, all participants are involved only in a single trial run and are not asked to repeat their trials. Nevertheless, we observe that most participants achieve higher success rates with the increasing number of trials. Therefore, the number of trials is limited to 20 to be able to validate the performance of the electromagnetic-based haptic interface. This problem can be partially overcome by increasing the number of participants, while keeping the same number of trials per each participant fixed, to validate the performance of the system. We also observe that most of the participants move their hand outside the workspace of the electromagnetic-based haptic interface. Therefore, it is essential to increase the magnetic field gradient of the system and also increase the magnetic dipole of the orthopedic finger splint attached to their fingers.

We construct the confusion matrix (Table IV) to show the predicted shapes (row) by the participants against actual shapes (column) [14]. This matrix reveals the ability of the system to render similar geometries that might confuse the participants. It shows the shapes that are most frequently

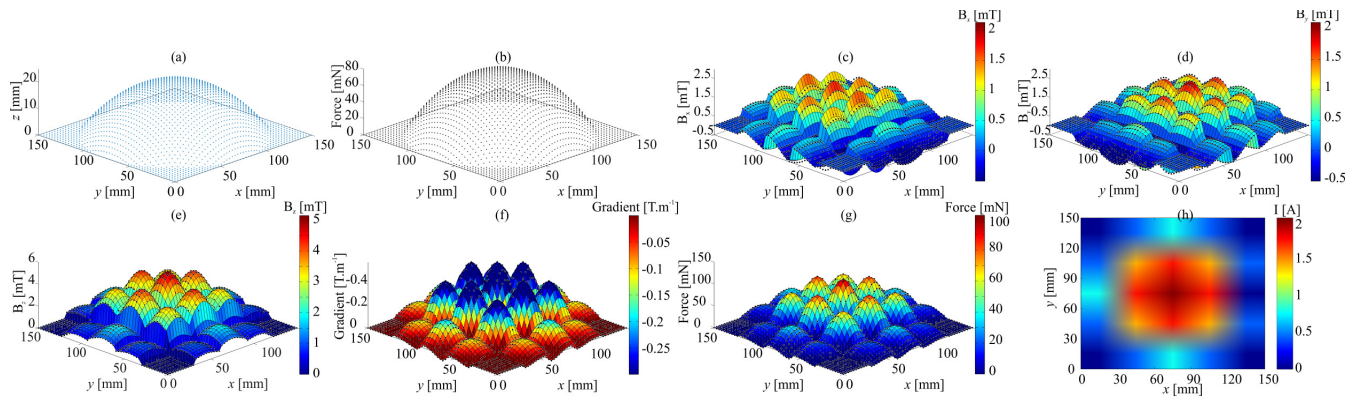


Fig. 6. Magnetic rendering of a hemisphere is achieved. The hemisphere is rendered from a sphere with diameter of 300 mm and its center is located at  $-130$  mm along  $z$ -axis (a) The surface constraint ( $g(x, t)$ ) of the hemisphere is decomposed into 2601 points. (b) The constraint force (6) is calculated based on the surface constraint and the scalar  $\lambda$ . (c, d, and e) Magnetic fields along  $x$ -,  $y$ -, and  $z$ -axis are calculated using (2) based on the constraint force. (f) The magnetic field gradient is also generated using (2). (g) Magnetic forces are calculated and generated using (4) and (5). (h) The current inputs to the coils are calculated using (9). The rendering index of the hemisphere is 0.27 mN.

confused across all the participants. The probability of error increases when we provide two similar geometries for the same test (e.g., hemisphere and hemicylinder). The percentage of predicting a hemisphere for a correct shape of hemicylinder is 40%, and the percentage of predicting hemicylinder for a correct shape of hemisphere is 39%. This confusion is due to two reasons. First, the limited range of this experiment (0 to 20 mm) along  $z$ -axis does not enable the participants to feel the difference between the two geometries. Second, the utilization of single dipole moment does not allow the participant to make a correct decision (each participant slides his finger differently to detect the geometry). This problem can be partially overcome by using magnetic orthopedic finger splint for each finger.

## VI. CONCLUSIONS AND FUTURE WORK

An electromagnetic-based haptic interface is developed and evaluated experimentally. The system consists of an array of electromagnetic coils and provides controlled magnetic force to an orthopedic finger splint to render 3D virtual objects. The system is experimentally evaluated by ten participants ( $n=200$ ) and success rate of 61% is demonstrated in distinguishing between the 3D virtual objects. However, our statistical analysis shows that the ability of the participants to distinguish between different geometries is not statistically significant, at 95% confidence level. We attribute this result to the limited number of electromagnetic coils within the electromagnetic configuration and the utilization of single magnetic dipole to sense the rendered magnetic forces. In addition, the number of trials of each participant is limited to validate the performance of the system, and this limitation influences our statistical analysis.

As part of future studies, we will increase the number of magnetic dipoles within the wearable haptic device (or utilize orthopedic finger splints for each finger) and incorporate a position sensing device to our electromagnetic-based haptic interface to detect the position of each dipole moment. Our control system will be modified to model the relation be-

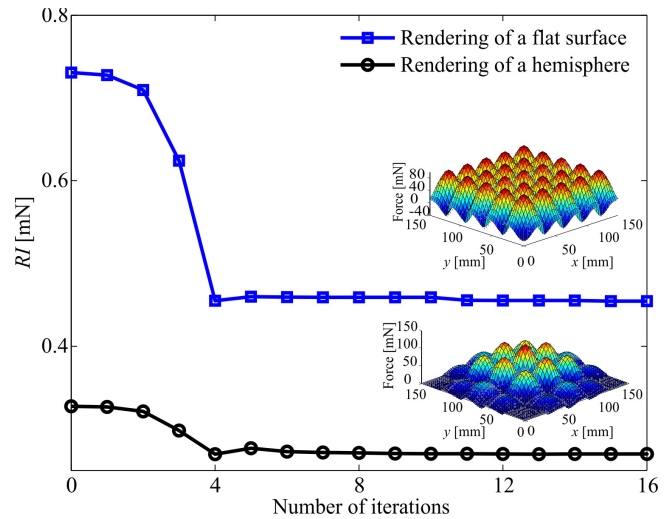
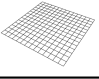
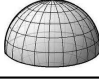
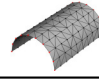



Fig. 7. Optimization of the current input using (9) is achieved and convergence is observed after 4 iterations. The optimization is performed using the Levenberg-Marquardt algorithm from MATLAB 8.4 (R2014b, The MathWorks, Inc., Massachusetts, USA). The rendering index ( $RI$ ) of the flat surface and hemisphere are 0.45 and 0.27, respectively (calculated using (11)).  $RI$  indicates the ability of the system to render virtual objects.

tween the current input and the magnetic force of each magnetic dipole [24]. It is also necessary to measure the magnetic forces during each rendering trial, and hence miniature force sensors will be incorporated between the wearable haptic device and the permanent magnets. It is likely that magnetic rendering will be used in surgical simulation training and other biomedical applications, where physicians interact with 3D virtual models for soft or deformable material such as soft tissue and bodily fluids. Therefore, our control system will be modified to enable rendering 3D dynamic geometries in real-time in the presence of position and force feedback from multiple dipole moments. This modification is necessary to allow the operator to interact with objects that undergo deformations upon interaction.

TABLE III

EXPERIMENTAL RESULTS OF MAGNETIC RENDERING OF 4 REPRESENTATIVE THREE-DIMENSIONAL (3D) VIRTUAL OBJECTS. TEN PARTICIPANTS EXPERIMENTALLY DEMONSTRATE 61% SUCCESS RATE ( $n=200$ ) IN DISTINGUISHING THE FOUR 3D GEOMETRIES. STATISTICAL ANALYSIS PROVIDES P-VALUE=0.15, AND INDICATES THAT THE DIFFERENCES BETWEEN THE RENDERED SHAPES ARE NOT SIGNIFICANT.

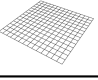
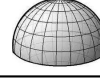
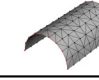

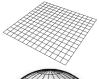
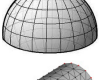
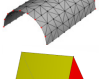

Object				
Participant   <i>RI</i>	0.45	0.27	0.39	0.23
1	1.0	0.8	0.8	0.6
2	0.6	0.8	0.4	0.4
3	0.6	0.8	0.0	0.6
4	1.0	0.2	0.8	1.0
5	0.8	0.4	0.8	1.0
6	0.0	0.4	0.2	1.0
7	1.0	0.2	0.8	0.8
8	0.8	0.4	0.6	0.0
9	0.6	0.6	0.6	0.6
10	0.8	0.4	0.4	0.8

## REFERENCES

- [1] D. A. Lawrence, "Stability and transparency in bilateral teleoperation," *IEEE Transactions on Robotics and Automation*, vol. 9, no. 5, pp. 624–637, October 1993.
- [2] X. L. K. Kim, Y. Zhang, and Y. Sun, "Nanonewton force-controlled manipulation of biological cells using a monolithic MEMS microgripper with two-axis force feedback," *Journal of Micromechanics and Microengineering*, vol. 18, no. 5, April 2008.
- [3] I. S. M. Khalil, Y. Michel, B. Su, and S. Misra, "Feeling paramagnetic micro-particles trapped inside gas bubbles: a tele-manipulation study," in *Proceedings of the International Conference on Manipulation, Manufacturing and Measurement on the Nanoscale (3M-NANO)*, pp. 225–230, Chongqing, China, July 2016.
- [4] Q. Zhang, H. Dong, and A. El Saddik, "Magnetic field control for haptic display: system design and simulation," *IEEE Access*, vol. 4, pp. 299–311, January 2016.
- [5] R. Traylor and H. Z. Tan, "Development of a wearable haptic display for situation awareness in altered-gravity environment: some initial findings," in *Proceedings of the IEEE Symposium on Haptic Interfaces for Virtual Environment and Teleoperator Systems*, pp. 159–164, February 2002.
- [6] H. Kim, C. Seo, J. Lee, J. Ryu, S. Yu, and S. Lee, "Vibrotactile display for driving safety information," in *Proceedings of IEEE Intelligent Transportation Systems Conference*, pp. 573–577, October 2006.
- [7] K. Minamizawa, D. Prattichizzo, and S. Tachi, "Simplified design of haptic display by extending one-point kinesthetic feedback to multi-point tactile feedback," in *Proceedings of IEEE Haptics Symposium*, pp. 257–260, March 2010.
- [8] D. Prattichizzo, F. Chinello, C. Pacchierotti, and M. Malvezzi, "Towards wearability in fingertip haptics: a 3-dof wearable device for cutaneous force feedback," *IEEE Transactions on Haptics*, vol. 6, no. 4, pp. 506–516, October 2013.
- [9] F. Arafsha, K. M. Alam, and A. El Saddik, "Design and development of a user centric affective haptic jacket," *Multimedia Tools and Applications*, pp. 1–18, November 2013.
- [10] Y. Suzuki and M. Kobayashi, "Air jet driven force feedback in virtual reality," *IEEE Transactions on Computer Graphics and Applications*, vol. 25, no. 1, pp. 44–47, January 2005.
- [11] R. Sodhi, I. Poupyrev, M. Glisson, and A. Israr, "Aireal: Interactive

TABLE IV

CONFUSION MATRIX [14] SHOWS THE PREDICTED VERSUS THE ACTUAL SHAPES. THE HEMISPHERE AND HEMICYLINDER ARE MOST FREQUENTLY CONFUSED ACROSS THE TEN PARTICIPANTS ( $n=200$ ).

Object				
	<b>37</b>	1	8	4
	7	<b>24</b>	17	2
	1	16	<b>26</b>	8
	8	2	6	<b>33</b>

- tactile experiences in free air," *ACM Transactions on Graphics*, vol. 32, no. 4, July 2013.
- [12] S. Gupta, D. Morris, S. N. Patel, and D. Tan, "Airwave: Non-contact haptic feedback using air vortex rings," in *Proceedings of ACM International Joint Conference on Pervasive and Ubiquitous Computing*, pp. 419–428, September 2013.
- [13] T. Hoshi, M. Takahashi, T. Iwamoto, and H. Shinoda, "Noncontact tactile display based on radiation pressure of airborne ultrasound," *IEEE Transactions on Haptics*, vol. 3, no. 3, pp. 155–165, February 2010.
- [14] B. Long, S. A. Seah, T. Carter, and S. Subramanian, "Rendering volumetric haptic shapes in mid-air using ultrasound," *ACM Transactions on Graphics*, vol. 33, no. 6, pp. 181 (1–10), November 2014.
- [15] M. Weiss, C. Wacharamanatham, S. Voelker, and J. Borchers, "Finger-flux: near-surface haptic feedback on tabletops," in *Proceedings of the ACM Annual Symposium on User Interface Software and Technology*, pp. 615–620, October 2011.
- [16] P. Berkelman, M. Miyasaka, and J. Anderson, "Co-located 3D graphic and haptic display using electromagnetic levitation," in *Proceedings of IEEE Haptics Symposium*, pp. 77–81, March 2012.
- [17] J. B. Brink, A. J. Petruska, D. E. Johnson, and J. J. Abbott, "Factors affecting the design of untethered magnetic haptic interfaces," *IEEE Haptics Symposium*, pp. 107–114, Houston, USA, February 2014.
- [18] D. Cappelleri, D. Efthymiou, A. Goswami, N. Vitoroulis, and M. Zavlanos, "Towards mobile microrobot swarms for additive micro-manufacturing," *International Journal of Advanced Robotic Systems*, vol. 11 (150), September 2014.
- [19] I. S. M. Khalil, R. M. P. Metz, B. A. Reefman, and S. Misra, "Magnetic-Based minimum input motion control of paramagnetic microparticles in three-dimensional space," in *Proceedings of the IEEE/RSJ International Conference of Robotics and Systems (IROS)*, pp. 2053–2058, Tokyo, Japan, November 2013.
- [20] I. S. M. Khalil, R. M. P. Metz, L. Abelman, and S. Misra, "Interaction force estimation during manipulation of microparticles," in *Proceedings of the IEEE/RSJ International Conference of Robotics and Systems (IROS)*, pp. 950–956, Vilamoura, Algarve, Portugal, October 2012.
- [21] J. J. Abbott, O. Ergeneman, M. P. Kummer, A. M. Hirt, and B. J. Nelson, "Modeling magnetic torque and force for controlled manipulation of soft-magnetic bodies," *IEEE Transactions on Robotics and Automation*, vol. 23, no. 6, pp. 1247–1252, December 2007.
- [22] M. P. Kummer, J. J. Abbott, B. E. Kartochvil, R. Borer, A. Sengul, and B. J. Nelson, "OctoMag: an electromagnetic system for 5-DOF wireless micromanipulation," *IEEE Transactions on Robotics*, vol. 26, no. 6, pp. 1006–1017, December 2010.
- [23] G. C. Burdea, "Haptic feedback for virtual reality," *Virtual Reality and Prototyping Workshop*, Laval, France, June 1999.
- [24] I. S. M. Khalil, L. Abelman, and S. Misra, "Magnetic-Based motion control of paramagnetic microparticles with disturbance compensation," *IEEE Transactions on Magnetics*, vol. 50, no. 10 (5400110), October 2014.